Fluorite-type materials in the monolayer limit

Shota Ono[1,*] and Ravinder Pawar[2]

[1] *Institute for Materials Research, Tohoku University, Sendai 980-8577, Japan*
[2] *Department of Chemistry, National Institute of Technology (NIT) Warangal, Warangal, Telangana, 506004, India*

The 2H, 1T, and their distorted structures are known as prototype structures of AB_2 monolayers. Here, we study a puckered structure that is truncated from the (110) surface of fluorite-type materials. 53 fluorite-type materials are investigated based on first-principles approach. The formation energy calculations indicate that seven systems form the puckered structure in the monolayer limit, while other systems form either 1T, 2H, or distorted 1T structures. The puckered structures of PbF_2, PRh_2, and Ga_2Au exhibit negative Poisson's ratio (NPR) in the out-of-plane direction. An analytical model for the NPR is derived. The surface energy calculations predict the appearance of NPR.

I. INTRODUCTION

Two-dimensional (2D) transition metal dichalcogenides have attracted attention due to their electronic, optical, and mechanical properties [1]. They are classed as AB_2 materials, where A is a transition metal and B is a chalcogen atom (S, Se, and Te), and exfoliated from 3D bulk due to their layered structure. They usually adopt either 2H or 1T structures and exhibit a structure-dependent property. For example, 2H MoS_2 is a semiconductor with a direct band gap, whereas 1T MoS_2 is a metal and shows a ferromagnetism under a tensile strain [2]. Distorted 1T structures have been studied in several AB_2 monolayers. The 1T′ structure is a Peierls distorted phase, and 1T′ WTe_2 shows a ferroelasticity that originates from the three equivalent directions of the distortion [3]. More complex geometries, such as 1T″ and 1T‴ structures, have also been investigated [4]. By performing high-throughput density-functional theory (DFT) calculations and assuming these structures, several structure maps have been proposed for AB_2 monolayers [5–7].

It is of fundamental importance to explore other structures different from 1T and related-structures. Recently, 2D materials created from non-layered materials have also been synthesized experimentally [8–10]. In addition, a wide variety of 2D materials has been predicted by cutting surfaces of non-layered materials. Lucking *et al.* have predicted that an ultrathin layer truncated from the (111) surface of zincblend-type semiconductors relaxes to double-layered honeycomb structure, and exhibits topological electronic band structure [11]. Friedrich *et al.* have studied electronic, optical, and magnetic properties of hematite and ilmenite in the monolayer limit [12]. The present authors have also studied structural and physical properties of 2D metallic systems [13–15]. Many elemental metals have hexagonal structures that are truncated from the (111) surface of the face-centered cubic structure or the (0001) surface of the hexagonal close-packed structure.

Fluorite-type (CaF_2-type) materials exhibit a cubic structure with a stoichiometry of AB_2, where A atoms form a face-centered cubic structure and B atoms occupy the tetrahedral sites. Therefore, two monolayer structures are truncated from their surface with keeping the stoichiometry of bulk (see Fig. 1(a)). One is the 1T structure that is truncated from the (111) surface. The other monolayer is truncated from the (110) surface and exhibits a highly puckered (PCK) structure. Although the PCK structure has been investigated theoretically for Be_2C [17] and ZrS_2 [18], such a structure is not the ground state. In addition, physical properties intrinsic to the PCK structure have not been explored yet.

In this paper, we investigate the structural and physical properties of 53 fluorite-type materials in the monolayer limit by using first-principles approach. Seven monolayers are identified to have the PCK structure,

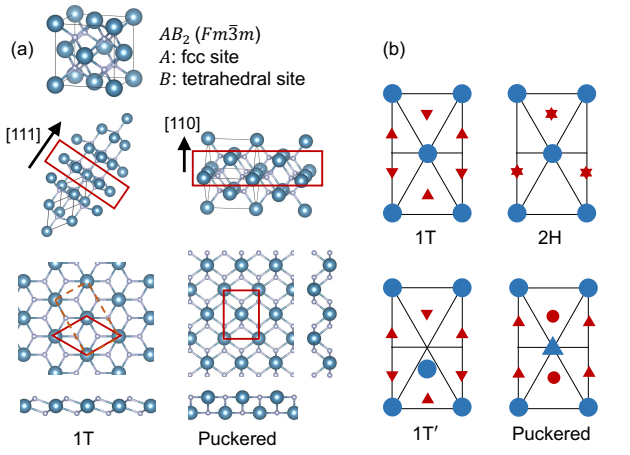

FIG. 1. (a) Crystal structure of fluorite-type material in the bulk form and the monolayer limit. 1T and puckered structures are truncated from the (111) and (110) surfaces, respectively. `VESTA` [16] is used to visualize crystal structures. (b) Schematic illustration of rectangular-shaped unit cell for 1T, 2H, 1T′, and PCK structures. Blue and red shapes indicate A and B atoms, respectively. Upward (downward) triangle is located above (below) $z = 0$ plane, and a circle is located at $z = 0$.

* shota.ono.d3@tohoku.ac.jp

and among them, PbF_2, Ga_2Au, and PRh_2 monolayers have an out-of-plane negative Poisson's ratio (NPR), that is, their thickness increases when stretched. PbF_2 and Ga_2Au monolayers are dynamically and thermodynamically stable, but PRh_2 monolayer is unstable at room temperature. By developing an analytical model, we demonstrate that the NPR is inherently present in the PCK structure. We also show that a linear relationship holds between the (111) and (110) surface energies, and PbF_2, Ga_2Au, and PRh_2 exhibit an anomalously small (110) surface energy.

It is known that many puckered structures exhibit a negative Poisson's ratio in the out-of-plane direction. For example, phosphorene (-0.027) [19, 20], arsenic (-0.09) [21], GeS (-0.14 within GGA-PBE and -0.19 with van der Waals correction) [22], SnSe (-0.17) [23], TiN (-0.102) [24], Ag_2S (-0.52) [25], and SnS_2 (-1.79) [26], where the value in a parenthesis indicates the Poisson's ratio ν at equilibrium condition. The Ga_2Au (-0.6) and PbF_2 (-0.4) monolayers studied in the present work also serve as 2D auxetic materials.

II. COMPUTATIONAL DETAILS

A. 2D structures

By using Materials Project database [27] and pymatgen code [28], we first extracted 94 fluorite-type materials (spacegroup of $Fm\bar{3}m$). These materials have been found in inorganic crystal structure database (ICSD). We excluded f-electron systems (lanthanide and actinide compounds), some of hydrogen compounds (Li_2NH, K_2PtH_4, $Ca_2RhH_{5.4}$, and Sr_2RhH_5), high-temperature phase materials (Cu_2S, Cu_2Se, and Al_2O), and oxides (PbO_2 and BiO_2). H_2S and H_2Se were also excluded because of a large discrepancy between experimental and calculated lattice constants. Zirconia (ZrO_2) and hafnia (HfO_2) in the fluorite-type structure are known to be stable above 2650 K and 2870 K, respectively [29], but these are studied in the present work.

We study 53 fluorite-type materials that consist of AB_2 (19), A_2B (14), and others (20), where A is a metallic element and B is H, F, Cl, O, S, Se, and Te. The AB_2-type system includes hydrides (8), fluorides (7), chlorides (2), and oxides (2). The A_2B materials consist of alkali metals A = Li (4), Na (4), K (3), and Rb (3) and chalcogen atoms B = O, S, Se, and Te. The other materials consist of alkali earth metals Be (2) and Mg (4) and other metallic elements Rh (2), Ir (2), Pt (4), Au (3), Ni (1), Co (1), and Pd (1).

We consider four crystal structures in the monolayer limit: 1T, 2H, 1T′, and PCK structures. These are illustrated in Fig. 1(b). The 1T structure corresponds to a monolayer that is truncated from the (111) surfaces of 3D phase. The 1T and 2H structures have a hexagonal unit cell with lattice constant a. The atoms are located at $A(0,0,0)$, $B(0,a/\sqrt{3},h)$, and $B(a/2,a/(2\sqrt{3}),-h)$ for 1T structure, and $A(0,0,0)$, $B(0,a/\sqrt{3},\pm h)$ for 2H structure, where $2h$ is the thickness of the monolayer. For the case of A_2B systems, A and B atoms should be interchanged. The 1T′ structure has a rectangular unit cell with lattice constants of a and b. This is regarded as a distorted 1T structure, as A atoms are dimerized along y direction and B atoms follow the movement of A atoms. The 1T′ structure may be buckled along the z direction. The PCK structure is regarded as a monolayer truncated from the (110) surface. A atom in the center of rectangular cell is displaced to z direction, i.e., $A(a/2,b/2,\delta)$. Each A atom is surrounded by four B atoms in the same planes, $z=0$ and δ.

B. First-principles calculations

We used Quantum ESPRESSO (QE) code [30] to perform density-functional theory (DFT) calculations. We used exchange-correlation energy functional within generalized-gradient approximation (GGA) parametrized by Perdew, Burke, and Ernzerhof (PBE) [31]. The electron-ion interactions were treated by using ultrasoft pseudopotentials in pslibrary1.0.0 [32]. The energy cutoff for wavefunction was set to be $E_{\rm cut}=\max(E_A,E_B)$ plus 20 Ry, where $E_j (j=A,B)$ is the suggested value for atom j, and the energy cutoff for charge density was set to be $10E_{\rm cut}$. Spin-polarized calculations were performed. A vacuum layer was set to be 15 Å for 2D systems. Convergence thresholds for the total energy in the self-consistent field calculations was set to be 10^{-12} Ry, and those for the total energy and forces for structure optimization were set to be 10^{-5} Ry and 10^{-4} a.u., respectively.

We first optimized the crystal structure by using smearing parameter of 0.015 Ry [33] and k-point distance Δk smaller than 0.1 Å^{-1}. The lattice constant of $0.95a_{3D}/\sqrt{2}$ was assumed as an initial guess for 1T and 2H structures, where a_{3D} is the lattice constant of the cubic phase and the factor of 0.95 accounts for the in-plane contraction due to the lack of atoms along the out-of-plane direction. For 1T′ structure, an initial structure was prepared by referring to the crystal structure of WTe_2 monolayer. For PCK structure, $b/a\simeq\sqrt{2}$ and $\delta=0.4a$ were assumed as an initial guess. Ferromagnetic phase was assumed in the initial spin configurations. For semiconducting systems, we optimized the structure again by using no smearing parameters and assuming $\Delta k\le 0.15$ Å^{-1}.

The stability of A_nB_m system is studied by calculating the formation energy

$$E_{\rm form}(A_nB_m)=\frac{\varepsilon_\alpha(A_nB_m)-n\varepsilon(A)-m\varepsilon(B)}{n+m}, \quad (1)$$

where n and m are integers, $\varepsilon_\alpha(A_nB_m)$ is the total energy of A_nB_m in the structure α, and $\varepsilon(X)$ with $X=A,B$ is the total energy of element X. To obtain $\varepsilon(X)$, we extracted the ground state structure of X from the

Open Quantum Materials Database (OQMD) [34], as done in the construction of Computational 2D Materials Database (C2DB) [35]. We optimized the structure and calculated $\varepsilon(X)$.

For the bulk and the 2D system having negative formation energy and the lowest energy among four structures (1T, 2H, 1T′, and PCK), we calculate the phonon dispersions within density-functional perturbation theory [36]. The long-range Coulomb correction is included in the force constant matrix for semiconductors. The Coulomb interaction in the z direction is truncated for 2D systems [37]. The $8 \times 8 \times 1$ q grid is used for the 1T and 2H structures, $6 \times 4 \times 1$ for the 1T′ and PCK structures, while $4 \times 4 \times 4$ for the 3D structure. The variable for the acoustic sum rule is set to be "crystal" [30].

For the systems having NPR, first-principles molecular dynamics (MD) simulations are performed by using QE [30]. A $4 \times 4 \times 1$ supercell is assumed, the volume of the unit cell is fixed, and the ionic temperature is kept to 300 K by adapting the velocity scaling. The Newton's equation is integrated by using the Verlet algorithm with a time step of 1 fs.

To investigate the ionic character of 2D AB_2 and A_2B systems, we estimate the Madelung constant M of 1T and 2H structures. The M is then characterized by h/a only. The electrostatic energy is calculated by using pymatgen code [28].

We calculate the surface energy γ for the (111) and (110) planes of fluorite-type materials. This is defined as

$$\gamma = \frac{E_{\rm slab} - nE_{\rm bulk}}{2A}, \tag{2}$$

where $E_{\rm slab}$ is the total energy of the slab including n unit cells, $E_{\rm bulk}$ is the total energy of 3D bulk, and A is the area of the surface. The factor of 1/2 accounts for the presence of two surfaces on top and bottom sides of the slab. For the (111) and (110) surfaces, 7 and 9 layer-thick slabs (21 and 27 atoms) including a vacuum layer of 15 Å are assumed and the atomic position of the middle (fourth and fifth) layer is fixed in the geometry optimization. The slab models are constructed by using atomic simulation environment (ASE) package [38].

III. RESULTS AND DISCUSSION

A. Stability trend

Before studying the 2D systems, we calculated phonon dispersions of 53 compounds in the fluorite structure to check whether the methodology used in the present work correctly predicts the dynamical stability of 3D counterparts. We have found that HgF_2, PIr_2, ZrO_2, and HfO_2 are unstable within PBE. When Perdew-Zunger [39] and PBEsol [40] functionals are used, HgF_2 and PIr_2 are dynamically stable.

Table I, II, and III lists the $E_{\rm form}$ of AB_2, A_2B systems, and other ordered alloys, respectively, in the 1T, 2H, 1T′, and PCK structures for 53 compounds. The $E_{\rm form}$ of bulk is also tabulated in these Tables. For AB_2 and A_2B systems except for ScH_2, YH_2, TiF_2, PbF_2, and Li_2Te, 1T phase is the most stable 2D structure because 2H and PCK phases are higher in energy and 1T′ phase is relaxed to 1T structure, as listed in Table I and II. The $E_{\rm form}$ of the 1T phase is larger than of bulk by less than 0.2 eV, while hydrides tend to be less stable. These 1T phases are dynamically stable. However, some of them show imaginary frequencies around Γ point in the Brillouin zone. This is attributed to an instability against the flexural (out-of-plane) vibrations. Phonon dispersions for the lowest energy phase are provided in Supplemental Materials [41].

TABLE I. Formation energy (eV/atom) of 3D bulk, 1T, 2H, 1T′, and Puckered (PCK) structures for 19 AB_2 systems. When 1T structure is not a ground state among 2D phases, the value is underlined for the most stable structure. A hyphen indicates that no scf convergence or relaxed geometry are obtained.

	bulk	1T	2H	1T′	PCK
ScH_2	−0.67	−0.27	−0.20	−0.27	<u>−0.29</u>
YH_2	−0.71	−0.25	−0.19	−0.25	<u>−0.29</u>
TiH_2	−0.48	−0.16	−0.05	−0.16	−0.10
ZrH_2	−0.56	−0.15	−0.02	−0.15	−0.10
VH_2	−0.20	0.02	0.11	0.02	0.12
NbH_2	−0.24	0.09	0.19	0.09	0.19
TaH_2	−0.10	0.16	0.22	0.16	0.24
CrH_2	0.06	0.17	0.25	0.17	-
CaF_2	−3.92	−3.79	−3.53	−3.79	−3.75
SrF_2	−3.93	−3.75	−3.52	−3.75	−3.73
BaF_2	−3.87	−3.69	−3.50	−3.69	−3.68
TiF_2	−2.72	−2.62	<u>−2.84</u>	−2.80	-
CdF_2	−2.17	−2.09	−1.90	−2.09	−2.06
HgF_2	−1.38	−1.33	−1.18	−1.33	−1.31
PbF_2	−2.37	−2.23	−2.08	−2.26	<u>−2.28</u>
$SrCl_2$	−2.50	−2.45	−2.31	−2.45	−2.42
$BaCl_2$	−2.58	−2.47	−2.34	−2.47	−2.46
ZrO_2	−3.38	−3.23	−2.68	−3.23	−3.19
HfO_2	−3.58	−3.46	−2.86	−3.46	−3.40

The stability preference of ordered alloys is different from AB_2 and A_2B systems. As listed in Table III, the 1T′ or PCK phases are preferred rather than 1T phase. However, many of them have positive $E_{\rm form}$, while they have negative $E_{\rm form}$ in the bulk. The systems having negative $E_{\rm form}$ are X_2Pt (X = Al, Ga, In, and Sn) in the 1T′ structure, PRh_2, Ga_2Au, and $CoSi_2$ in the PCK structure, and Al_2Pd in the 2H structure. These structures are all dynamically stable except for Sn_2Pt. The phonon dispersions are provided in Supplemental Materials [41].

We next calculate the Madelung constant M to study the ionic character of AB_2 and A_2B systems. The hydrides are excluded due to the metallic band structure.

TABLE II. Same as Table I but for 14 A_2B-type systems.

	bulk	1T	2H	1T′	PCK
Li_2O	−1.86	−1.69	−1.38	−1.69	−1.65
Li_2S	−1.36	−1.16	−0.94	−1.16	−1.15
Li_2Se	−1.27	−1.08	−0.88	−1.08	−1.08
Li_2Te	−1.04	−0.86	−0.70	−0.85	−0.86
Na_2O	−1.22	−1.08	−0.86	−1.08	−1.04
Na_2S	−1.08	−0.90	−0.71	−0.90	−0.88
Na_2Se	−1.08	−0.89	−0.72	−0.89	−0.88
Na_2Te	−0.94	−0.76	−0.61	−0.76	−0.76
K_2S	−1.08	−0.93	−0.78	−0.93	−0.91
K_2Se	−1.11	−0.96	−0.82	−0.96	−0.94
K_2Te	−1.03	−0.88	−0.74	−0.88	−0.86
Rb_2S	−1.02	−0.90	−0.76	−0.90	−0.87
Rb_2Se	−1.07	−0.94	−0.81	−0.94	−0.91
Rb_2Te	−1.01	−0.87	−0.74	−0.87	−0.85

TABLE III. Same as Table I but for 20 ordered alloys.

	bulk	1T	2H	1T′	PCK
Be_2C	−0.24	0.21	0.82	0.56	0.21
Be_2B	0.04	0.45	0.56	0.53	0.45
Mg_2Si	−0.16	0.30	0.34	0.28	0.27
Mg_2Ge	−0.27	0.17	0.20	0.19	0.13
Mg_2Sn	−0.20	0.21	0.49	0.15	0.16
Mg_2Pb	−0.07	0.32	0.55	0.25	0.24
$AsRh_2$	−0.42	0.44	0.40	0.29	0.25
PRh_2	−0.75	0.06	0.06	−0.01	−0.06
PIr_2	−0.37	0.75	0.46	0.40	0.45
Sn_2Ir	−0.25	0.22	0.23	0.06	0.21
Al_2Pt	−0.89	−0.22	−0.05	−0.29	−0.22
Ga_2Pt	−0.58	−0.12	−0.02	−0.23	−0.14
In_2Pt	−0.48	−0.02	0.01	−0.13	−0.08
Sn_2Pt	−0.45	−0.08	−0.07	−0.18	−0.13
Al_2Au	−0.44	0.09	0.13	0.11	0.10
Ga_2Au	−0.24	0.10	0.06	0.04	−0.01
In_2Au	−0.25	0.12	0.07	0.03	0.01
Si_2Ni	−0.36	0.21	0.15	0.13	0.01
$CoSi_2$	−0.53	0.18	0.15	0.08	−0.06
Al_2Pd	−0.61	−0.01	−0.15	−0.13	−0.01

We assume the oxidation states of B^- for halogens (F and Cl) and and B^{2-} for chalcogens (O, S, Se, and Te). Figure 2 plots M as a function of h/a for AB_2 and A_2B systems. The 1T structures have $h/a \in [0.15, 0.32]$ and $M > 2.3$, whereas the 2H structures have $M < 2.3$. Therefore, the ionic character of 1T structure is more significant than of 2H structure.

Note that TiF_2 monolayer has a large value of $h/a = 0.48$ and prefers 2H structure. It is interesting that 2H

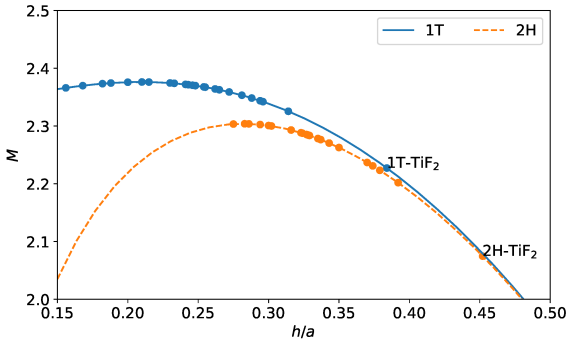

FIG. 2. The Madelung constant M of 1T (solid) and 2H (dashed) structures as a function of h/a. The circles indicate M of 25 systems listed in Table I and II except for hydrides. TiF_2 has a large h/a, and M is small compared to the other compounds.

TiF_2 is more stable than the 3D bulk [42] (see Table I). The 2H structure has an indirect band gap of 1.3 eV (PBE) from K to Γ in the Brillouin zone, while the 1T structure is metallic. This relationship between the crystal structure and electronic property is similar to that in MoS_2 monolayer [2]. Such a structure-property relationship reflects the electronic configuration of transition metals. For Ti atom $[Ar](3d)^2(4s)^2$, and a possible oxidation state is Ti^{2+}. For Mo atom $[Kr](4d)^5(5s)^1$, and a possible oxidation state is Mo^{4+} by assuming S^{2-}. The remaining two electrons in the Ti and Mo atoms should be occupied into d energy levels. As the 2H structure has the D_{3h} symmetry, d_{z^2} state becomes the lowest energy state. By considering the spin degeneracy, the d_{z^2} state is completely filled, while the other d states are empty, resulting in a finite band gap. On the other hand, the 1T structure has the O_h symmetry, and d_{xy}, d_{yz}, and d_{zx} states become stable in energy. These states are partially filled with two electrons, resulting in a metallic phase.

As we have obtained stable structures of fluorite-type materials in the monolayer limit, we next explore physical properties of PCK structures below.

B. Negative Poisson's ratio

We study the elastic property of the PCK structures: ScH_2, YH_2, PbF_2, Li_2Te, PRh_2, Ga_2Au, and $CoSi_2$. The PCK structure is stretched along the y direction. We define the out-of-plane strain as $\varepsilon_z = (d - d_0)/d_0$, where d and d_0 are the thickness of the monolayer with and without the strain, respectively. Figure 3(a) shows ε_z as a function of ε_y. The atom position and the lattice constant a are optimized, while the lattice constant b is fixed. Interestingly, when ε_y is increased, ε_z also increases for Ga_2Au, PbF_2, and PRh_2 monolayers. This indicates an NPR in the out-of-plane direction, $\nu = -\partial\varepsilon_z/\partial\varepsilon_y < 0$. As shown in Fig. 3(b), ν takes a minimum value of −0.8

at $\varepsilon_y = 0.02$ in Ga_2Au monolayer. First-principles MD simulations show that they are thermodynamically stable at 300 K except for PRh_2, as shown in Fig. 3(c). For the case of 2D semiconductors (PbF_2 and Li_2Te), we plotted the potential energy and ε_z as functions of $(a-a_0)/a_0$ and $(b-b_0)/b_0$, where a_0 and b_0 are the lattice constants in equilibrium. The NPR is observed only when the PbF_2 monolayer is stretched along the y direction. This is provided in the Supplemental Material [41].

We have investigated whether the NPR also appears for thicker PbF_2 films. The PCK structure is constructed by stacking two PbF_2 layers [see Fig. 1(a)]. Therefore, we have constructed three (9 atoms) and four (12 atom) PbF_2 layers. The strain is increased from $\varepsilon_y = 0$ to 0.06. However, no NPR is observed in these systems because the thickness monotonically decreases from 4.017 and 6.134 Å to 3.947 and 6.056 Å for three and four layers, respectively.

1. Analytical model

We discuss an origin of the NPR based on an analytical model. As shown in Fig. 3(d), the atomic positions of the PCK structure are denoted as $A_1(0,0,0)$, $A_2(a/2,b/2,z_A)$, $B_1(0,b/4,z_B)$, and $B_2(a/2,b/4,z_A-z_B)$, where z_A and z_B are the z coordinates of A_2 and B_1 atoms, respectively, and B_2 atom has $z = z_A - z_B$. The thickness is given by $d = 2z_B - z_A$ when $z_A < z_B$. When the monolayer is elongated along the y direction ($\varepsilon_y > 0$), it will be contracted along the x direction ($\varepsilon_x < 0$), and the A_2 and B_1 atoms will approach the $z = 0$ plane ($\varepsilon_z^A < 0$ and $\varepsilon_z^B < 0$). Then, the z coordinate of B_2 atom becomes negatively large, which results in an increase in d, *i.e.*, the NPR.

To show this, we assume that the bond lengths, $l(A_1A_2), l(A_1B_1)$, and $l(A_1B_2)$, are not changed under the strain. This is a good approximation for the PCK structures: For PbF_2, $l(A_1A_2) = 4.02 \to 4.06$ Å, $l(A_1B_1) = 2.33 \to 2.35$ Å, and $l(A_1B_2) = 2.57 \to 2.58$ Å when $\varepsilon_y = 0.06$ is applied. The structural parameters are changed from a, b, z_A, and z_B to $a' = a(1+\varepsilon_x)$, $b' = b(1+\varepsilon_y)$, $z'_A = z_A(1+\varepsilon_z^A)$, and $z'_B = z_B(1+\varepsilon_z^B)$, respectively. When $l(A_1A_2)$ is equal to $l'(A_1A_2)$ under the strain, the following equation should be satisfied:

$$a^2\varepsilon_x + b^2\varepsilon_y + 4z_A^2\varepsilon_z^A = 0, \tag{3}$$

where the first order of strains is considered. From the conditions $l(A_1B_1) = l'(A_1B_1)$ and $l(A_1B_2) = l'(A_1B_2)$, we obtain the relationships

$$b^2\varepsilon_y + 16z_B^2\varepsilon_z^B = 0 \tag{4}$$

and

$$4a^2\varepsilon_x + b^2\varepsilon_y + 16(z_A - z_B)(z_A\varepsilon_z^A - z_B\varepsilon_z^B) = 0. \tag{5}$$

Eq. (4) indicates that the z coordinate of B_1 atom decreases to $z_B(1+\varepsilon_z^B)$ because $\varepsilon_z^B < 0$ when $\varepsilon_y > 0$. From Eqs. (3)-(5), we obtain

$$\varepsilon_z^A = -\frac{b^2}{16z_Az_B}\left(4 - \frac{z_A}{z_B}\right)\varepsilon_y. \tag{6}$$

This also predicts $\varepsilon_z^A < 0$ because $z_A \simeq z_B$. The ε_z^A is negatively larger than ε_z^B by a factor of three. Therefore, the thickness, expressed by

$$d = d_0 + \frac{b^2}{8z_B}\left(1 - \frac{z_A}{2z_B}\right)\varepsilon_y \tag{7}$$

with $d_0 = 2z_B - z_A$, increases with ε_y. This results in $\nu = -\partial(d/d_0)/\partial\varepsilon_y < 0$. For an unrelaxed PCK structure ($b = \sqrt{2}a$ and $d_0 = z_A = z_B = a/2$), ν is exactly equal to $-1/2$.

In our model, $\nu < 0$ always holds. In realistic systems, the bond lengths are changed within a few percent under the strains. In addition, B_1 and B_2 atoms have different y coordinates. These affects the ε_y-dependence of ν.

2. Relationship to the surface energy

Our analytical model suggests that the NPR is inherently present in the PCK structure. As the PCK structure is truncated from the (110) surface, it is interesting to study whether the monolayers having NPR are identified by surface energy calculations.

Figure 4 shows a correlation of the surface energies between the (111) and (110) surfaces. The γ for AB_2 and A_2B systems is plotted in Fig. 4(a), while that for the other ordered alloys is plotted in Fig. 4(b). The calculated data for ZrO_2, HfO_2, Li_2O, and Be_2O are plotted in Fig. 4(b) due to the large γ. CrH_2 is excluded because the scf calculation assuming ferromagnetic phase is not converged. For all systems, the (111) surface is more stable. This is consistent with previous calculations on CaF_2, SrF_2, and BaF_2 [43]. As shown in Fig. 4(a), a linear relationship of $\gamma_{(110)} \simeq 1.5\gamma_{(111)}$ holds for AB_2 and A_2B systems. For the other ordered alloys in the high energy regime ($\gamma_{(111)} \gtrsim 0.4$ J/m^2), the relation $\gamma_{(111)} < \gamma_{(110)} \lesssim 1.5\gamma_{(111)}$ is satisfied, as shown in Fig. 4(b). It is noteworthy that PbF_2, Ga_2Au, and PRh_2 having NPR exhibit a large deviation from the linear relationship of $\gamma_{(110)} \simeq 1.5\gamma_{(111)}$.

IV. CONCLUSION

We have studied 53 fluorite-type materials in the monolayer limit by performing first principles calculations. Most of AB_2 and A_2B systems form the 1T structure. The puckered structure can exhibit a negative Poisson's ratio (NPR) in the out-of-plane direction. An analytical model is developed to explain the NPR. The puckered structures having NPR (PbF_2, Ga_2Au, and PRh_2) are identified by the energy difference between the (111) and (110) surfaces.

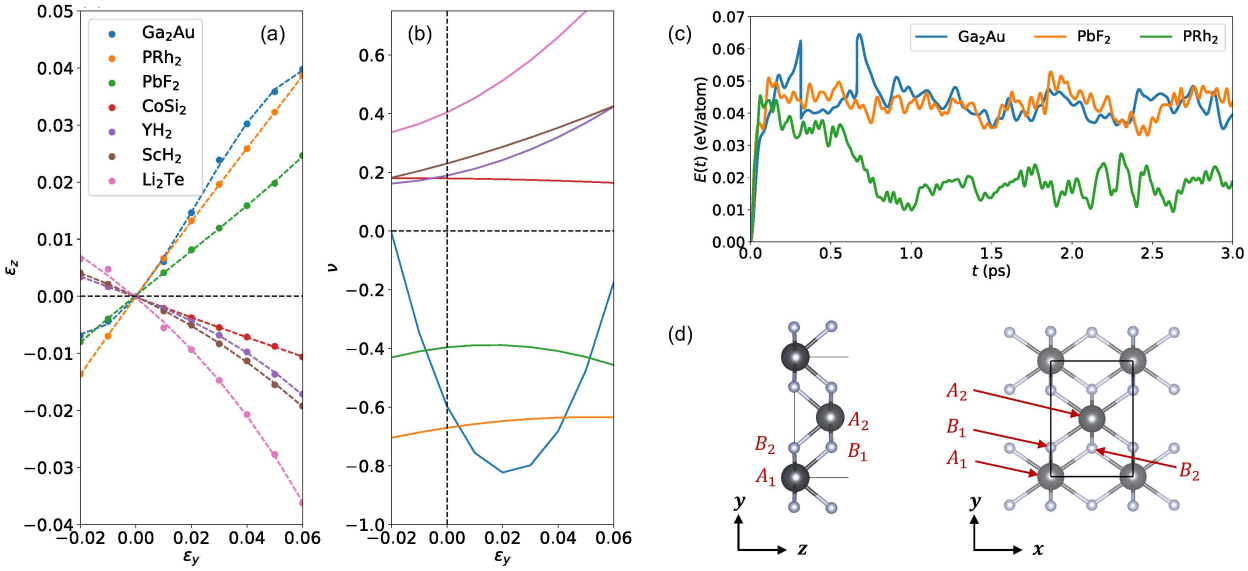

FIG. 3. The ε_y-dependence of (a) the out-of-plane strain ε_z and (b) the Poisson's ratio $\nu = -\partial\varepsilon_z/\partial\varepsilon_y$ for the PCK structures. The third order polynomial is fitted to points $(\varepsilon_y, \varepsilon_z)$, and ν is obtained from the derivative of the polynomial with respect to ε_y. (c) MD runs at 300 K for Ga_2Au, PbF_2, and PRh_2 monolayers in the PCK phase. A $4 \times 4 \times 1$ supercell is assumed (96 atoms). PRh_2 monolayer becomes unstable after 1 ps. (d) A_1, A_2, B_1, and B_2 atoms for the PCK-structured AB_2 monolayer (see Sec. III B 1).

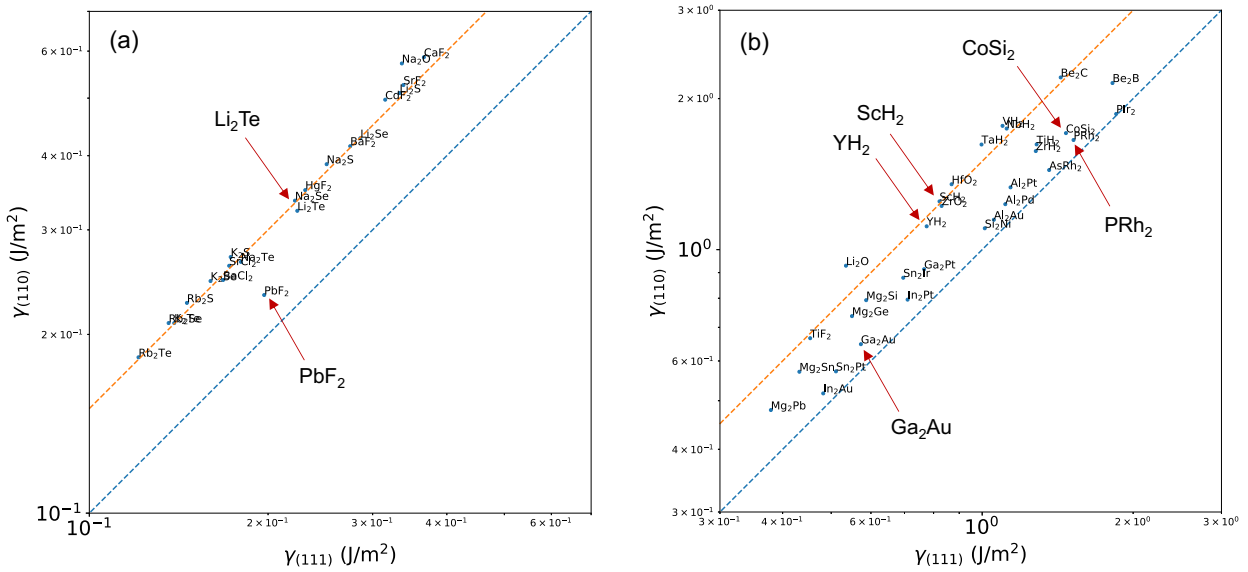

FIG. 4. Correlation between $\gamma_{(111)}$ and $\gamma_{(110)}$. The dashed lines indicate $\gamma_{(110)} = \gamma_{(111)}$ (blue) and $\gamma_{(110)} = 1.5\gamma_{(111)}$ (orange).

In the present work, we have focused on non-layered fluorite-type materials to explore novel 2D materials. The 1T and puckered structures are truncated from the (111) and (110) surfaces, respectively. A similar strategy, truncation from low-index surfaces of non-layered materials, will be useful to expand the family of 2D materials.

ACKNOWLEDGMENTS

This work was supported by JSPS KAKENHI (Grant No. 21K04628). Calculations were done using the facilities of the Supercomputer Center, the Institute for Solid State Physics, the University of Tokyo, and the Supercomputer "MASAMUNE-IMR" at Center for Computa-

tional Materials Science, Institute for Materials Research, Tohoku University.

[1] W. Choi, N. Choudhary, G. H. Han, J. Park, D. Akinwande, and Y. H. Lee, Recent development of two-dimensional transition metal dichalcogenides and their applications, Mater. Today, **20**, 116 (2017).

[2] W. Xu, S. Yan, and W. Qiao, Magnetism in monolayer 1T-MoS_2 and 1T-MoS_2H tuned by strain, RSC Adv. **8**, 8435 (2018).

[3] W. Li and J. Li, Ferroelasticity and domain physics in two-dimensional transition metal dichalcogenide monolayers, Nat. Commun. **7**, 10843 (2016).

[4] W. Zhao, J. Pan, Y. Fang, X. Che, D. Wang, K. Bu, and F. Huang, Metastable MoS_2: Crystal Structure, Electronic Band Structure, Synthetic Approach and Intriguing Physical Properties, Chem. Eur. J. **24**, 15942 (2018).

[5] M. Fukuda, J. Zhang, Y.-T. Lee, and T. Ozaki, A structure map for AB_2 type 2D materials using high-throughput DFT calculations, Mater. Adv. **2**, 4392 (2021).

[6] A. Silva, J. Cao, T. Polcar, and D. Kramer, Pettifor maps of complex ternary two-dimensional transition metal sulfides, Npj Comput. Mater. **8**, 178 (2022).

[7] P. Kumar, V. Sharma, S. N. Shirodkar, and P. Dev, Predicting phase preferences of two-dimensional transition metal dichalcogenides using machine learning, Phys. Rev. Materials **6**, 094007 (2022).

[8] D. Ji, S. Cai, T. R. Paudel, H. Sun, C. Zhang, L. Han, Y. Wei, Y. Zang, M. Gu, Y. Zhang, W. Gao, H. Huyan, W. Guo, D. Wu, Z. Gu, E. Y. Tsymbal, P. Wang, Y. Nie, and X. Pan, Freestanding crystalline oxide perovskites down to the monolayer limit, Nature **570**, 87 (2019).

[9] A. B. Puthirath, A. P. Balan, E. F. Oliveira, V. Sreepal, F. C. Robles Hernandez, G. Gao, N. Chakingal, L. M. Sassi, P. Thibeorchews, and G. Costin et al., Apparent gerromagnetism in exfoliated ultrathin pyrite sheets, J. Phys. Chem. C **125**, 18927 (2021).

[10] A. P. Balan, A. B. Puthirath, S. Roy, G. Costin, E. F. Oliveira, M. A. S. R. Saadi, V. Sreepal, R. Friedrich, P. Serles, and A. Biswas et al., Non-van der Waals quasi-2D materials; Recent advances in synthesis, emergent properties and applications, Mater. Today **58**, 164 (2022).

[11] M. C. Lucking, W. Xie, D.-H. Choe, D. West, T.-M. Lu, and S. B. Zhang, Traditional Semiconductors in the Two-Dimensional Limit, Phys. Rev. Lett. **120**, 086101 (2018).

[12] R. Friedrich, M. Ghorbani-Asl, S. Curtarolo, and A. V. Krasheninnikov, Data-Driven Quest for Two-Dimensional Non-van der Waals Materials, Nano Lett. **22**, 989 (2022).

[13] S. Ono, Dynamical stability of two-dimensional metals in the periodic table, Phys. Rev. B **102**, 165424 (2020).

[14] S. Ono, Two-dimensional square lattice polonium stabilized by the spin-orbit coupling, Sci. Rep. **10**, 11810 (2020).

[15] A. A. Sangolkar, S. Jha, and R. Pawar, Density Functional Theory-Based Calculations for 2D Hexagonal Lanthanide Metals, Adv. Theory Simul. **5**, 2200057 (2022).

[16] K. Momma and F. Izumi, VESTA 3 for three-dimensional visualization of crystal, volumetric and morphology data, J. Appl. Crystallogr. **44**, 1272 (2011).

[17] M. Naseri, J. Jalilian, F. Parandin, and K. Salehi, A new stable polycrystalline Be_2C monolayer: A direct semiconductor with hexa-coordinate carbons, **382**. 2144 (2018).

[18] M. M. Abutalib, A DFT based prediction of a new 2D zirconium disulfide *Pmmm*-ZrS_2 monolayer: A quasi direct band gap semiconductor, Results Phys. **12**, 903 (2019).

[19] J. W. Jiang and H. S. Park, Negative poisson's ratio in single-layer black phosphorus, Nat. Commun. **5**, 4727 (2014).

[20] Y. Du, J. Maassen, W. Wu, Z. Luo, X. Xu, and P. D. Ye, Auxetic black phosphorus: a 2D material with negative Poisson's ratio, Nano Lett. **16**, 6701 (2016).

[21] J. Han, J. Xie, Z. Zhang, D. Yang, M. Si, and D. Xue, Negative Poisson's ratios in few-layer orthorhombic arsenic: First-principles calculations, Appl. Phys. Express **8**, 041801 (2015).

[22] L. C. Gomes, A. Carvalho, and A. H. Castro Neto, Enhanced piezoelectricity and modified dielectric screening of two-dimensional group-IV monochalcogenides, Phy. Rev. B **92**, 214103 (2015).

[23] L. C. Zhang, G. Qin, W. Z. Fang, H. J. Cui, Q. R. Zheng, Q. B. Yan, and G. Su, Tinselenidene: a Two-dimensional Auxetic Material with Ultralow Lattice Thermal Conductivity and Ultrahigh Hole Mobility, Sci. Rep. **6**, 19830 (2016).

[24] L. Zhou, Z. Zhuo, L. Kou, A. Du, and S. Tretiak, Computational Dissection of Two-Dimensional Rectangular Titanium Mononitride TiN: Auxetics and Promises for Photocatalysis, Nano Lett. **17**, 4466 (2017).

[25] R. Peng, Y. Ma, Z. He, B. Huang, L. Kou, and Y. Dai, Single-Layer Ag_2S: A Two-Dimensional Bidirectional Auxetic Semiconductor, Nano Lett. **19**, 1227 (2019).

[26] H. Wang, T. Li, Z. Chen, W. Zhu, W. Lin, H. Wang, X. Liu, and Z. Li, High out-of-plane negative Poisson's ratios and strong light harvesting in two-dimensional SiS_2 and its derivatives, Nanoscale **15**, 16155 (2023).

[27] A. Jain, S. P. Ong, G. Hautier, W. Chen, W. D. Richards, S. Dacek, S. Cholia, D. Gunter, D. Skinner, G. Ceder, and K. A. Persson, The Materials Project: A materials genome approach to accelerating materials innovation, APL Mater. **1**, 011002 (2013).

[28] S. P. Ong, W. D. Richards, A. Jain, G. Hautier, M. Kocher, S. Cholia, D. Gunter, V. L. Chevrier, K. A. Persson, and G. Ceder, Python Materials Genomics (pymatgen): A robust, open-source python library for materials analysis, Comput. Mater. Sci. **68**, 314 (2013).

[29] H. Shin, A. Benali, Y. Luo, E. Crabb, A. L. Bezanilla, L. E. Ratcliff, A. M. Jokisaari, and O. Heinonen, Zirconia and hafnia polymorphs: Ground-state structural properties from diffusion Monte Carlo, Phys. Rev. Materials **2**, 075001 (2018).

[30] P. Giannozzi, O. Andreussi, T. Brumme, O. Bunau, M. B. Nardelli, M. Calandra, R. Car, C. Cavazzoni, D. Ceresoli, and M. Cococcioni *et al.*, Advanced capabilities for materials modeling with Quantum ESPRESSO, J. Phys.: Condens. Matter **29**, 465901 (2017).

[31] J. P. Perdew, K. Burke, and M. Ernzerhof, Generalized Gradient Approximation Made Simple, Phys. Rev. Lett.

77, 3865 (1996).
[32] A. Dal Corso, Pseudopotentials periodic table: From H to Pu, Computational Material Science **95**, 337 (2014).
[33] M. Methfessel and A. T. Paxton, High-precision sampling for Brillouin-zone integration in metals, Phys. Rev. B **40**, 3616 (1989).
[34] S. Kirklin, J. E. Saal, B. Meredig, A. Thompson, J. W. Doak, M. Aykol, S. Rühl, and C. Wolverton, The Open Quantum Materials Database (OQMD): assessing the accuracy of DFT formation energies, Npj Comput. Mater. **1**, 15010 (2015).
[35] M. N. Gjerding, A. Taghizadeh, A. Rasmussen, S. Ali, F. Bertoldo, T. Deilmann, U. P. Holguin, N. R. Knøsgaard, M. Kruse, A. H. Larsen *et al.*, Recent Progress of the Computational 2D Materials Database (C2DB), 2D Materials **8**, 044002 (2021).
[36] S. Baroni, S. Gironcoli, A. Dal Corso, and P. Giannozzi, Phonons and related crystal properties from density-functional perturbation theory, Rev. Mod. Phys. **73**, 515 (2001).
[37] T. Sohier, M. Calandra, and F. Mauri, Density functional perturbation theory for gated two-dimensional heterostructures: Theoretical developments and application to flexural phonons in graphene, Phys. Rev. B **96**, 075448 (2017).
[38] A. H. Larsen, J. J. Mortensen, J. Blomqvist, I. E. Castelli, R. Christensen, M. Dułak, J. Friis, M. N. Groves, B. Hammer, C. Hargus *et al.*, The atomic simulation environment—a Python library for working with atoms, J. Phys.: Condens. Matter **29**, 273002 (2017).
[39] J. P. Perdew and A. Zunger, Self-interaction correction to density-functional approximations for many-electron systems. Phys. Rev. B **23**, 5048 (1981).
[40] J. P. Perdew, A. Ruzsinszky, G. I. Csonka, O. A. Vydrov, G. E. Scuseria, L. A. Constantin, X. Zhou, and K. Burke, Restoring the Density-Gradient Expansion for Exchange in Solids and Surfaces, Phys. Rev. Lett. **100**, 136406 (2008).
[41] See Supplemental Material at (URL) for (a) phonon dispersions of 53 monolayers and (b) potential energy and ε_z as functions of in-plane lattice constants for PbF_2 and Li_2Te in the PCK structure.
[42] N. Morita, T. Endo, T. Sato, and M. Shimada, TiF_2 with fluorite structure — a new compound, J. Mater. Sci. Lett. **6**, 859 (1987).
[43] S. Bebelis and P. Nikolopoulos, Temperature Dependence of the Surface Energy of the Low-index Planes of CaF_2, BaF_2 and SrF_2, J. Mater. Eng. Perform. **26**, 1223 (2017).